Materials Research Proceedings 41 (2024) 1248-1258 https://doi.org/10.21741/9781644903131-139

Massive nitrogen super-saturation into CoCrMo Alloys for improvement of tribological performance

AIZAWA Tatsuhiko[1,a*], FUNAZUKA Tatsuya[2,b], SHIRATORI Tomomi[2,c] and SUZUKI Yohei[3,d]

[1]3-15-10 Minami-Rokugo, Ota-City, Tokyo 144-0045, Japan

[2]3190 Gofuku, Toyama-City, Toyama 930-8555, Japan

[3]942-2 Shiga-Kuwahara, Suwa-City, Nagano 392-0012, Japan

[a]taizawa@sic.shibaura-it.ac.jp, [b]funazuka@eng.u-toyama.ac.jp, [c]shira@eng.u-toyama.ac.jp, [d]y-suzuki@komatsuseiki.co.jp

Keywords: Plasma Nitriding, Cocrmo Alloys, Massive Nitrogen Interstitials, Low Friction and Wear

Abstract. The cobalt-chromium-molybdenum (CoCrMo) superalloys have been utilized in the dental, knee, and hip arthroplasty applications because of their unique combination of high strength, high wear and corrosion resistance. A massive nitrogen supersaturation (MNS) process was proposed as a surface treatment to improve these strength, hardness and ductility, further needed for hip replacement and dental prosthesis. CoCrMo disc specimens were prepared for plasma immersion nitriding at 673 K for 21.6 ks by 50 Pa. The nitrogen solute uniformly distributed in the MNS-layer with the average content of 5 mass%. Higher surface hardness than 1550 HV was attained under application of 10 N. The maximum friction coefficient was halved before and after MNS and this low frictional state with $\mu < 0.45$ was preserved although the sliding condition by 0.1 m/s.

Introduction

Cobalt-chromium (CoCr) and cobalt-chromium-molybdenum (CoCrMo) superalloys have been utilized in the dental, knee and hip arthroplasty applications because of their unique combination of high strength, high wear and corrosion resistance, and excellent fatigue strength [1]. Various studies were reported in literature to improve the hardness by multi-phase structuring [2], to attain higher tensile and fatigue strength by heat treatment [3], to overcome their intrinsic low ductility by enrichment of chromium and nitrogen [4], and to much improve the mechanical balancing among strength, hardness and ductility by surface treatment [5, 6]. In these approaches, the plasma nitriding processes were high-lighted to increase the surface hardness without loss of high corrosion toughness [7-9]. Among them, the low temperature plasma nitriding provided a way to make nitrogen supersaturation to CoCr and CoCrMo alloys with much higher nitrogen solute content than their intrinsic solubility limit [10].

Owing to this massive nitrogen supersaturation (MNS), the original surface hardness of 450 HV_{1N} was increased two to three times after plasma nitriding at 673 K for 14.4 ks (or 4 h). The average nitrogen content reached 5 mass% in the nitrided surface layer. To be noticed, this nitrogen supersaturated layer had an intensely textured microstructure with nearly the same orientation to (111) crystallographic orientation.

In the present study, this microstructure control effect on the mechanical properties of MNS-CoCrMo, is investigated by the hardness testing and tribotesting. First, the low temperature plasma nitriding conditions are described with the comments on the holding temperature and the mixture gas pressure. XRD, SEM-EDX, and EBSD are utilized to make microstructure analysis on the surface and cross-section of MNS-CoCrMo specimen. The hardness measurement and tribological

testing are employed to describe the mechanical and tribological behavior of MNS-CoCrMo and to discuss its possibility in working as a die for precise forging process.

Methods and Materials

The low temperature plasma nitriding system is explained for massive nitrogen supersaturation to CoCrMo specimen. Microstructure analysis and mechanical characterization is performed to investigate the relationship between the MNS-induced nanostructure and hardness as well as tribological performance,

Massive nitrogen supersaturation. The plasma carburizing system is schematically illustrated in Fig. 1a. With reference to the previous studies in [11-12], the hollow cathode device was employed to increase the nitrogen-ion and NH-radical densities more than 3 x 10^{17} ions/m^3 and to deepen the nitrogen supersaturated layer thickness. This system consisted of the RF (Radio Frequency) - and DC (Direct Current) - generators to independently ignite the nitrogen – hydrogen plasmas.

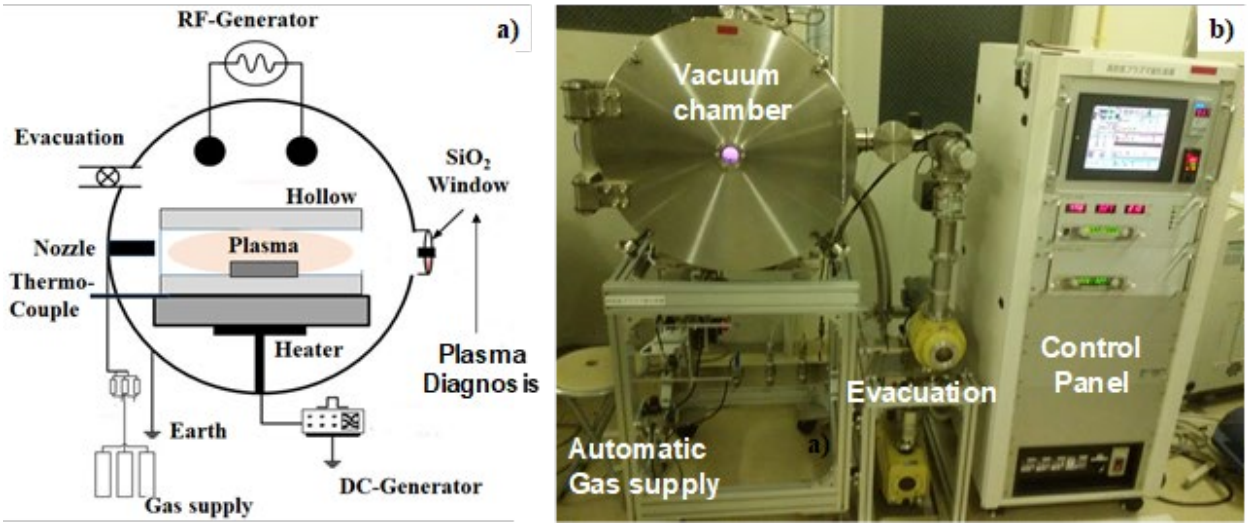

Fig. 1. Plasma immersion nitriding for massive nitrogen supersaturation. a) A schematic view on the experimental setup, and b) overview on the nitriding system.

This system in Fig. 1a consisted of the vacuum chamber, the evacuation unit, the RF-DC generators, the mixture gas supply of N_2 and H_2, the heating unit, and, the hollow cathode device. As shown in Fig. 1b, the specimen was placed in this hollow cathode setup for high densification of nitrogen ions, NH radicals and electrons. Both the hollow and the specimen were electrically connected to the same DC-bias. The ionization from the neutral molecules of N_2 and H_2 to the activated species {N^+, N*, NH} was enhanced in this hollow cathode setup. This enhancement of plasma density was controlled by the ratio of gas flow rate in N_2 + H_2. The yield of NH radicals and nitrogen ions (N^+) in the plasma sheath increases with decreasing H_2 flow rate after the quantitative plasma diagnosis in [11-12].

After setting the specimen into the hollow cathode setup, the chamber was evacuated down to 0.1 Pa, and, filled with the nitrogen gas until 100 Pa. Under this constant pressure, the specimen was presputtered at 673 K for 1.8 ks (or 0.5 h) with the DC-bias of -500 V. The plasma nitriding followed this pre-sputtering stage continuously. The specimen was plasma nitrided at 673 K for 21.6 ks (or 6 h) at 50 Pa. After the plasma diagnosis as stated in above, the plasma nitriding process parameters were controlled to have the RF voltage of 250V, the DC-bias of -500 V and the gas flow rate ratio of 160 ml/min for N_2 and 30 ml/min for H_2, respectively. After this nitriding process, the specimen was cooled down to RT in the chamber under the N_2 atmosphere

CoCrMo disc. The CoCrMo alloy rod (Cobarion; Eiwa, Co., Ltd., Iwate, Japan) was cut and sliced to the disc specimens with the diameter of 20 mm and the thickness of 5 mm. Each disc specimen was adjusted in dimension and mirror polished on its either surface. Its chemical composition was listed in Table 1. Its normal grain size in average was 20 ⌠m.

Table 1. Chemical composition of CoCrMo disc specimen for nitrogen supersaturation.

Element	Cr	Mo	Si	Mn	Fe	Ni	N	C	Co
Content	27.14	5.99	0.59	0.61	0.06	< 0.01	0.11	0.052	Balance

*mass%

Microstructural analysis. XRD (X-Ray Diffraction) was first utilized to describe the phase change before and after MNS. SEM (Scanning Electron Microscopy), EDX (Energy Dispersive X-ray spectroscopy) and EBSD (Electron Back-Scattering Diffraction) were used for microstructure analysis and element mapping on the surface and cross-section of MNS-CoCrMo disc specimens.

The cross-section of sample was mechanically polished by SiC sand paper with increasing the mesh-grades and by the alumina powder solution before finishing. The mirror-like surface condition was adjusted and finished below the mask by the ion milling (HITACH-IM400) with argon etching.

In EBSD analysis, IPF (Inverse Pole Figure) was mapped in the ND (Normal Direction), RD (Rolling Direction) and TD (Tangential Direction), respectively. The crystallographic structure was analyzed by this IPF. KAM (Kernel Angle Misorientation) was employed to describe the local plastic strain distribution in the MNS-specimen. Phase mapping was also utilized to analyze the effect of plastic straining to the transformation from γ-phase. The surface profile of nitrided specimen was observed by the optical microscopy and SEM.

Mechanical characterization. Micro-Vickers testing (Mitsutoyo, Co., Ltd.; Kanagawa, Japan) was employed to measure the surface hardness by varying the applied load. The hardness depth profile was also analyzed under the constant applied load by 10 N. Tribotesting (CVS; Switzerland) was utilized to measure the variation of friction coefficient with increasing the sliding distance up to L = 500 m. As depicted in Fig. 2a, the friction coefficient (⌠) was defined as follows; ⌠ = F / W for the measured shear force (F), and the applied normal load (W). As shown in Fig. 2b, the sliding speed (V) was kept constant by 0.1 m/s.

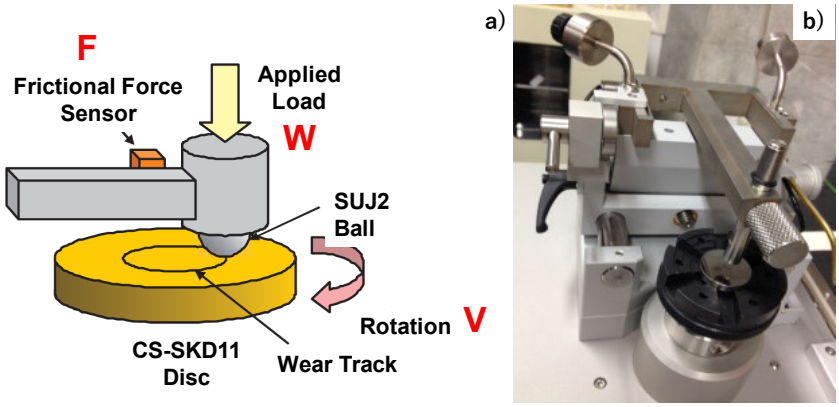

Fig. 2. Ball-on-disc tribological testing system. a) Schematic view on the rotational sliding test, and b) overview of testing system.

Results

The microstructure of MNS-CoCrMo discs at 673 K was analyzed on their surface and cross-section. Their crystallographic textures were investigated to describe the microstructural evolution through MNS. Micro-hardness testing was used to analyze the hardening behavior at the MNS-layer. Tribotesting was employed to prove that lower frictional state was preserved at the MNS-specimen than the bare CoCrMo alloys.

Microstructure analysis on the surface of NS-CoCrMo. High resolution optical microscopy was utilized to observe the MNS-layer surface with comparison to a bare CoCrMo disc. Fig. 3 depicts the overview of the MNS-CoCrMo specimen as well we the crystallographic structure. As explained before, the bare CoCrMo had a uniform microstructure with the average grain size of 20 ⌈m. On the other hand, as pointed by the white arrows in Fig. 3b, the most of grains with fine grain boundaries have a lot of fine skewed scratches on their surface with small-sized spouts. The original crystallographic structure with the average grain size of 20 ⌈m was significantly modified to have plastically deformed grains with fine slip-lines in each inside.

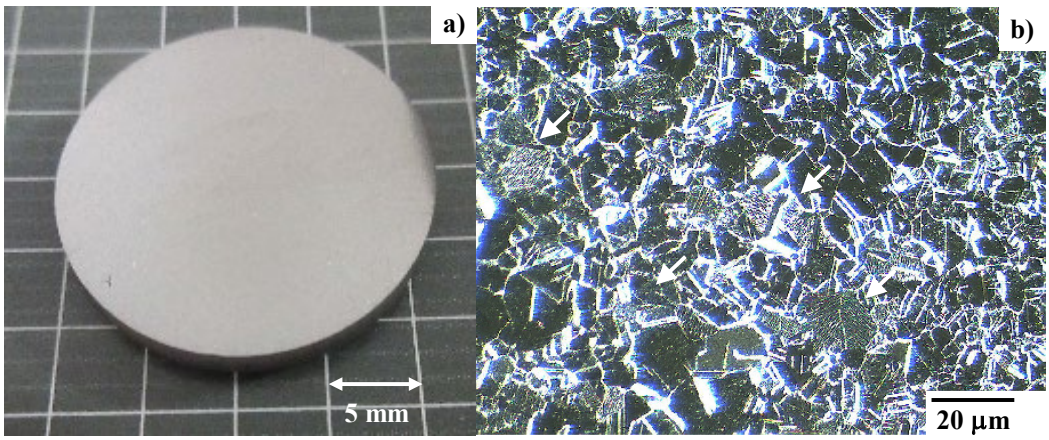

Fig. 3. Optical-microscopic image of CoCrMo disc after plasm immersion nitriding. a) Overview of MNS-CoCrMo disc, and b) microscopic image on its surface.

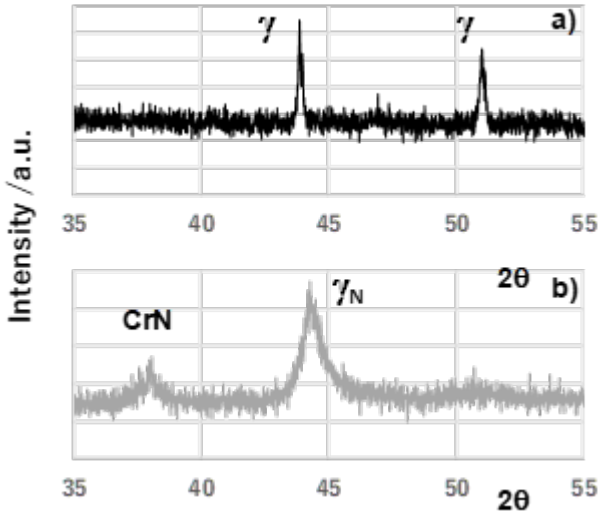

Fig. 4. Comparison of the XRD diagrams for CoCrMo discs before and after plasma immersion nitriding. a) XRD diagram before MNS, and b) XRD diagram after MNS.

XRD was utilized to describe the nitrogen supersaturation and the chromium nitride (CrN) formation via the plasma nitriding at 673 K for 21.6 ks. Fig. 4 compares the XRD diagrams between the bare and nitrided specimens. The XRD diagram for the bare CoCrMo alloy is characterized by two ©-phase peaks at 2θ = 44° and 2θ = 51°, respectively. Under the alloying design in Table 1, the CoCrMo alloy disc specimen had fully austenitic phase without ε-phases. The MNS-CoCrMo alloy has an expanded γ-phase with CrN in the trace level. After [13], the grain size of CrN was estimated from the measured full width half maximum of this CrN broad peak to be 10 nm.

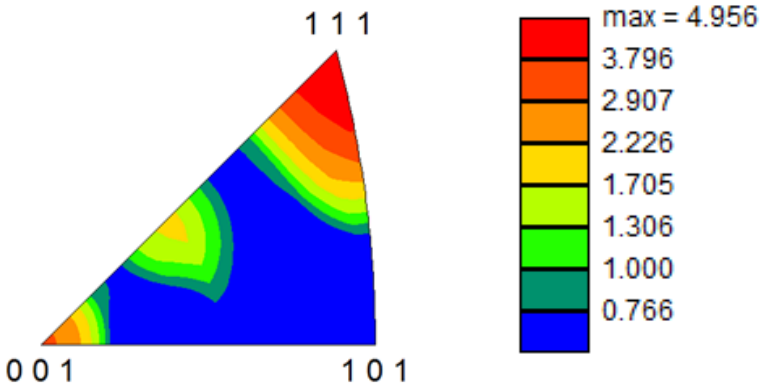

Fig. 5. The pole Fig. in ND (Normal Direction) on the MNS-CoCrMo by the texture analysis using EBSD.

EBSD was utilized to characterize the crystallographic surface structure on the MNS-CoCrMo disc. The pole figure in ND was shown in Fig. 5. MNS-CoCrMo is intensely textured to have a lot of nano-grains with the orientation to (111). Since the as-sliced CoCrMo disc from the rolled bar feedstock had no specific crystallographic orientations, this texturing must be induced by massive nitrogen supersaturation process.

Microstructure analysis on the cross-section of NS-CoCrMo. MNS-CoCrMo disc specimen was precisely cut to halves and polished for SEM-EDX analysis on the cross-sectional microstructure.

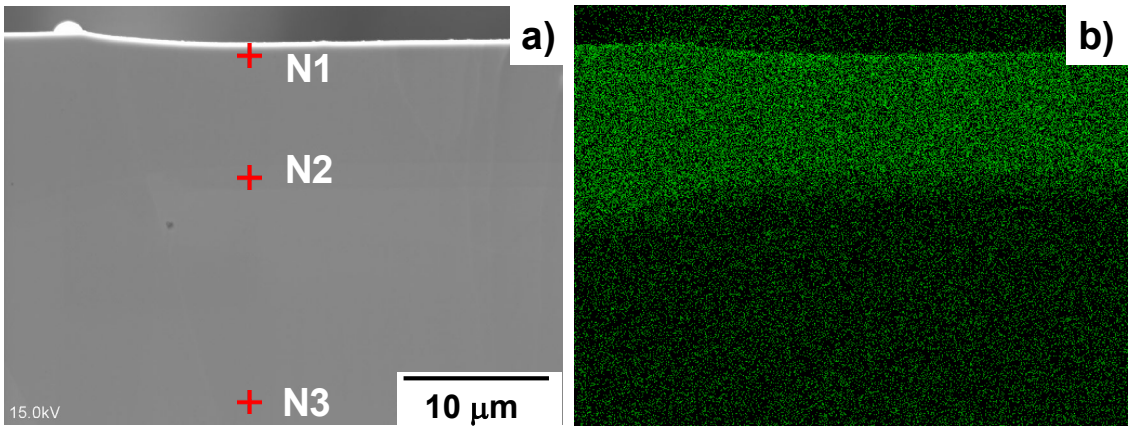

Fig. 6. SEM-EDX analysis on the cross-section of the MNS-CoCrMo disc. a) SEM image on the cross-section of MNS-layer across the nitriding front end, and b) nitrogen mapping from the surface to the depth.

Fig. 6a depicts the SEM image on the cross-section of MNS-CoCrMo. The MNS-layer was formed with the thickness of 12 ⌈m. As shown in Fig. 6b, the nitrogen solute homogeneously distributes from the surface to the depth of 12 ⌈m. The pointwise chemical composition analysis was performed at several positions from the surface to the depth; e.g., N_1 located at the vicinity of surface, N2 located just above the nitriding front end, and N3 located far from this nitriding front end. At these positions, the contents of Co, Cr, Mo, Si and N were measured to be nearly constant at every position on the cross-section; e.g., [Co] ~ 60 mass%, [Cr] ~ 25 mass%, [Mo] ~ 6.5 mass%, and [Si] =0.6 mass%. The nitrogen content [N] distributes from the surface to the depth as depicted in Fig. 7.

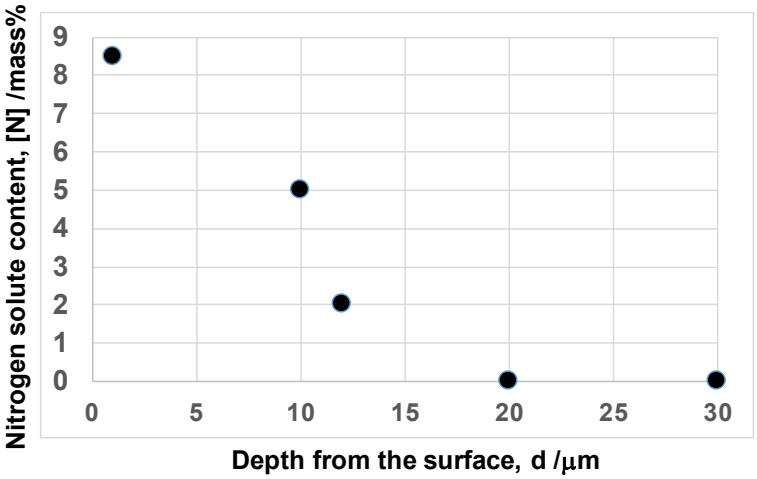

Fig. 7. Nitrogen solute content [N] from the surface to the depth across the nitriding front end.

In the MNS-layer, the nitrogen content is more than 5 mass%. This [N] gradually decreases with the depth (d) across the nitriding front end. No nitrogen solute was detected when d > 15 ⌈m. This high nitrogen content in the surface layer proves that nitrogen solute is massively saturated in the depth of CoCrMo specimen.

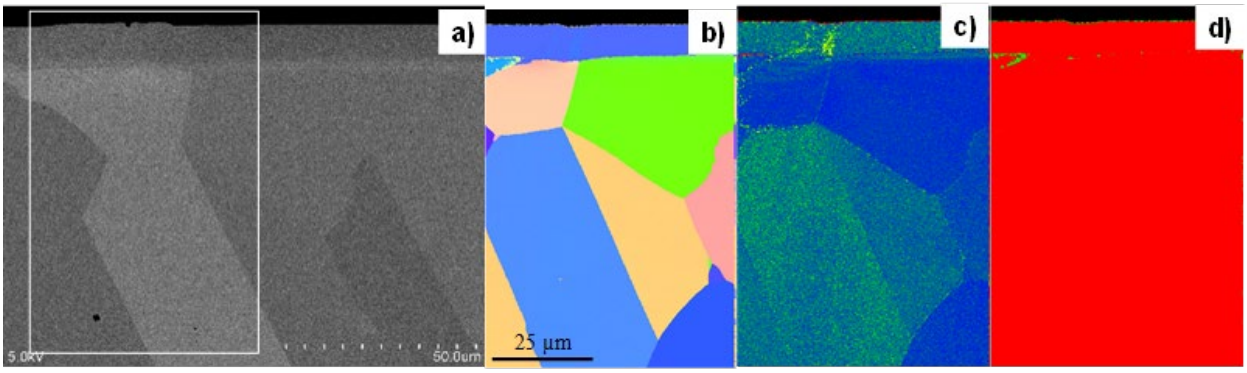

Fig. 8. SEM image, phase mapping, plastic strain distribution and granular structure analyzed respectively by EBSD on the cross-section. a) SEM image, b) inverse pole figure, c) plastic strain distribution, and d) phase mapping.

SEM image on the cross-section is depicted in Fig. 8a. The MNS-layer is formed as a mono-grain; no fine grain boundaries are detected in this layer. This implies that the impinged nitrogen solutes by MNS uniformly distribute in the MNS-layer and super-saturate the specimen irrespective to their chemical affinity to Cr, Co, and Mo. MNS below this layer, larger size grains than CoCrMo before MNS are aligned in the specified crystallographic orientation. Inverse pole

figure in ND is shown in Fig. 8b. The MNS-layer is intensely textured to have an orientation in (111). In the literature [9], the crystallographic texturing by the plasma nitriding was reported to vary itself with dependence on the bias voltage. Its intensity for crystallographic orientation was much weaker as seen in Fig. 8.

Let us investigate the effect of plastic straining on this change. As depicted in Fig. 8c, formation of MNS-layer accompanies with high plastic straining. Since the easy-to-straining orientation is (111), Fig.s 8b and 8c reveal that intense crystallographic texturing to (111) in MNS-layer is directly induced by the plastic straining during MNS. The original CoCrMo grains are also affected by plastic straining to change their crystallographic orientation. Fig. 8d shows the phase mapping in cross-section. Most domains in each grain preserve the same ©-phase as before MNS; phase transformation takes place at the nitriding front end. This phase change suggests that the original ©-grains are modified by MNS process to drive the crystallographic structure change.

Mechanical characterization. Micro-Vickers hardness and BOD testing procedures were utilized to describe the change of hardness and tribological behavior before and after MNS. The surface hardness change was first analyzed by varying the applied load up 20 N (or 2 kgf).

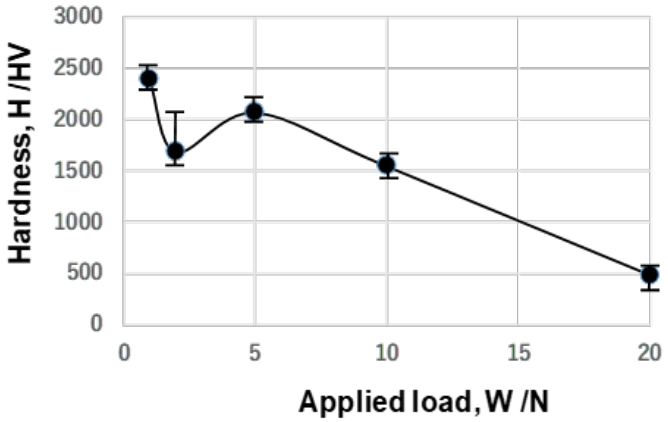

Fig. 9. Surface hardness change by varying the applied load for the NS-CoCrMo specimen at 673 K for 21.6 ks by 50 Pa.

As shown in Fig. 9, the surface hardness is higher than 1500 HV under application of 10 N. Since the hardness of bare CoCrMo is 450 $HV_{0.1N}$, the surface hardness increases by MNS three times or more. Let us consider the effect of penetration depth by indentation of diamond cone on the measured surface hardness in hardness testing. After [14], the surface hardness is affected by the substrate hardness when the penetration depth (D) is more than the surface layer thickness (h) in five to six times. When applying 1 N, D ~ 2 ⌈m; since MNS layer thickness is 12 ⌈m, h ~ 6 x D. Then, the measured hardness is equivalent to the hardness of MNS layer. With increasing W, the soft substrate hardness gradually affects onto the measured hardness. Monotonous decrease of the measured hardness with W in Fig. 9, proves this influence of substrate hardness to the measured hardness. In fact, when W = 20 N, the measured hardness becomes nearly equal to the substrate hardness. MNS-CoCrMo is characterized by this high hardness up to 2400 HV when applying 1N.

In literature [4, 7, 9], the high surface hardness was attained by nitrogen addition and plasma treatment. In most of those studies, the applied load was limited by 1 – 2 N; their maximum hardness at the vicinity of surface was also upper bound by 1100 HV. Higher hardness than 2000

HV_{1N} in Fig. 9 implies that MNS-layer with the specific crystallographic orientation to (111) has a unique mechanical property due to its nanostructure.

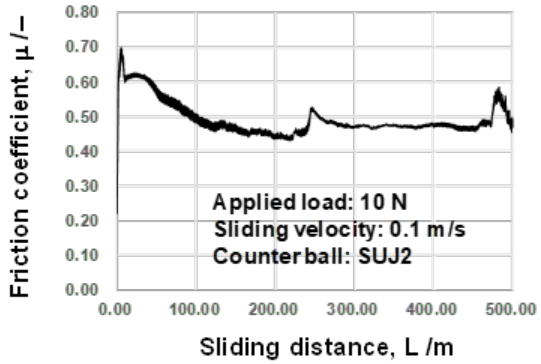

Fig. 10. Variation of the friction coefficient with increasing the sliding distance (L) up to L = 500 m for the bare CoCrMo.

BOD testing was employed to describe the change of tribological performance before and after MNS. Fig. 10 shows the variation of friction coefficient with increasing the sliding distance (L) for the bare CoCrMo disc. Even except for the initial high frictional behavior, the average friction coefficient is 0.45 to 0. 5 with a few metal-sticking or a spiky increase of ⌈. Large worn-out volume is experienced in this sliding mode testing in hard-to-hard materials. As suggested in [15], the friction coefficient as well as the specific wear volume are expected to decrease with hardening the die against the same counter materials. In this case, the normal hardness of SUJ2 is 700 HV. Then, this friction and wear behavior of bare CoCrMo alloys can be improved by MNS.

Fig. 11 shows the variation of friction coefficient with the sliding distance for MNS-CoCrMo. The maximum friction coefficient is reduced from 0.7 to 0.4. The low frictional state with ⌈ = 0.45 is preserved in the whole sliding distance without any spiky peaks. This assures that MNS-layer is useful to significantly lower the friction and wear.

To be noticed in Fig. 11, the small spiky increase of ⌈ might come from the surface roughness. This might be induced by the slip-lines as seen in Fig. 3b.

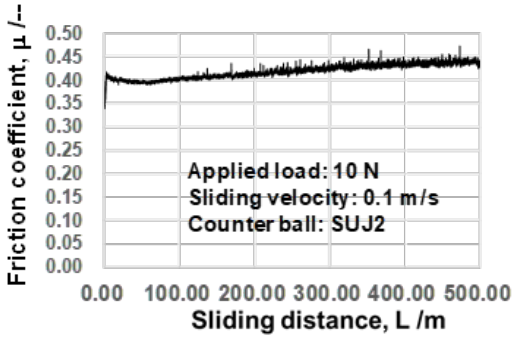

Fig. 11. Variation of the friction coefficient with increasing the sliding distance (L) up to L = 500 m for the NS-CoCrMo at 673 K for 21.6 ks by 50 Pa.

Discussion

The massive nitrogen supersaturation process is characterized by uniform distribution of nitrogen solute with high contents into CoCrMo substrate. Together with this supersaturation, CrN is slightly synthesized as a nano-sized precipitate in the MNS-CoCrMo. To be noticed in the microstructure change by MNS, the plastically strained nano-grains in Fig. 3 have intense textures

with nearly the same crystallographic orientation to (111). After EBSD analysis, the MNS-layer looks a single crystal with the common orientation to (111). KAM distribution in Fig. 8c proves that high plastic straining forms a dense slip-line field network into MNS-layer so that the modified nano-grains are forced to orient to the easy-to-plastically-deformation axis (111). As partially discussed in [9, 10], this specific crystallographic orientation by MNS must be dependent on the holding temperature and gas pressure in MNS.

Let us compare this MNS processes between the CoCrMo alloy and the AISI316. As studied in [16-17], the nitrogen-rich and nitrogen-poor clusters are microscopically formed in the MNS-AISI316 together with microscopic decomposition among the constituent elements of AISI316 or Fe, Cr and Ni with dependence on each different chemical affinity to nitrogen solute. This nanostructure change significantly influences on the mesoscopic analysis by EBSD; the original uniform austenitic structure changes itself to two-phase structure. On the other hand, almost all grains of MNS-CoCrMo have austenitic phase in Fig. 8d; no chemical decomposition occurs in MNS-layer of CoCrMo alloy. More precise description is expected by STEM analysis on MNS-CoCrMo to investigate the microscopic interaction among the constituent atoms of Co, Cr and Mo and the massively supersaturated nitrogen solutes.

Higher surface hardness than 2000 HV_{1N} reveals that hardening mechanism must be different from the normal one working in MNS-AISI316/304 and MNS-tool-steels. In addition to fine CrN precipitation in MNS-CoCrMo, the intensely textured $©_N$-grains work as a blockage of dislocation movements. Further studies on the effect of strongly textured $©_N$-nanograins on the hardness and strength are needed by using the nano-indentation and STEM analysis.

Higher hardness than 1550 HV_{10N} is also promising to apply this MNS-CoCrMo alloys to die-technology. As reported in [18], the bare CoCrMo was utilized as a die for hot extrusion of aluminum alloy with better performance. This highly hardened superalloy by MNS with preferable balancing among the strength, the ductility and the toughness, is useful for hot stamping and forging instead of the WC (Co) with coating.

The tribological data on the tool steel and high-speed steel dies against the SUJ2 were summarized in [19]. In every hard-to-hard material friction, much higher friction coefficients than 1.0 were referred in that data base. The low frictional behavior with $\mu < 0.45$ by the sliding movement by 0.1 m/s under 10 N or 1 kgf, proves that MNS-CoCrMo works as an artificial knee and hip part in medical applications.

Summary

Massive nitrogen supersaturation to CoCrMo alloys forms a uniform hardened layer up to 2400 HV with the high average nitrogen solute content of 5 mass% and the intensely textured crystallographic structure. Every nano-grain in this layer has common crystallographic orientation to (111) due to the slip-line field by the plastic straining during MNS. Hardness decreases gradually with increasing the penetration depth by indenter. This implies that nitrogen solute diffuses deeper than the MNS-layer thickness to modify the microstructure, neighboring to the nitriding front end. The tribological property is also improved by MNS. The friction coefficient is preserved to be less than 0.45 without any metallic sticking against the hard SUJ2 materials.

This significant improvement in mechanical property and performance by MNS assures that MNS-CoCrMo is useful as a new artificial part in the dental and knee-/hip-arthroplasty and as a die material for hot stamping and forging processes. In particular, MNS-CoCrMo is suitable to mold-stamping the oxide glass works into optical elements at the elevated holding temperature instead of WC (Co) and AISI316 steel molds.

Acknowledgment

The authors would like to express their gratitude to S-I. Kurozumi (Nano-Film Coat, llc.) and K. Kubota (Graduate School of Engineering, Toyama University) for their help in experiments.

References

[1] Bandyopaghyay, A., Traxel, K. D., Avila, J. D., Mitra, I., Bose. S., CoCr alloys. Biomaterials Science, 4th Ed. Academic Press 1.3.3C (2020) pp. 257-269. https://doi.org/10.1016/B978-0-12-816137-1.00020-9

[2] Carek, A.; Babic, J. Z., Schauperl, Z., Tomislav, B., Mechanical properties of Co-Cr alloys for metal base framework. Int. J. Prosthodont. Restor. Dent. 1 (2011) pp. 13-19. https://doi.org/10.5005/jp-journals-10019-1003

[3] Devine, T. M., Wulff, J., Cast vs. wrought cobalt-chromium surgical implant alloys. J. Biomed. Mater. Res. 9 (1975) pp. 151-167. https://doi.org/10.1002/jbm.820090205

[4] Lee, S., Nomura, N., Chiba, A., Significant improvement in mechanical properties of biomedical Co-Cr-Mo alloys with combination of N addition and Cr-enrichment. Materials Transactions. 2 (2008) pp.260-264. https://doi.org/10.2320/matertrans.MRA2007220

[5] Longquan, S.; Northwood, D., Cao, Z., The properties of a wrought biomedical Cobalt-Chromium alloy. J. Mat. Sci. 18 (1994) pp. 1233-1238. https://doi.org/10.1007/BF00975070

[6] Cheng, H.; Xu, M., Zhang, H., Wu, W., Zheng, M., Li, X., Cyclic fatigue properties of Cobalt-Chromium alloy clasps for partial removable dental protheses. J. Prosthetic Dent. 104 (2010) pp. 389-396. https://doi.org/10.1016/S0022-3913(10)60173-4

[7] Wang Q.; Zhang L., Shen H., Microstructure analysis of plasma nitrided cast/forged CoCrMo alloys. Surf. Coat. Technol. 205 (7) (2010) pp. 2654-2660. https://doi.org/10.1016/j.surfcoat.2010.10.031

[8] Dong H.; S-phase surface engineering of Fe-Cr, Co-Cr and Ni-Cr alloys. Int. Mater. Rev. 55 (2) (2011) pp. 65-98. https://doi.org/10.1179/095066009X12572530170589

[9] Shukla K.; Sugumaran A. A., Khan I., Ehiasarian A. P., Hovsepian P. E., Low pressure plasma nitrided CoCrMo alloy utilizing HIPIMS discharge for biomedical applications. J. Mech. Behavior of Biomedical Materials. 111 (2020) 104110. https://doi.org/10.1016/j.jmbbm.2020.104004

[10] Aizawa T.; Funazuka T., Shiratori T., Suzuki Y., Massive nitrogen supersaturation to CoCrMo alloys for surface microstructure control. Academia Mater. Sci. 1 (2023) pp. 1-9. https://doi.org/10.20935/AcadMatSci6139

[11] Farghali A., Aizawa T., Yoshino T., Microstructure/mechanical characterization of plasma nitrided fine-grain austenitic stainless steels in low temperature. Nitrogen 2 (2021) pp. 244-258. https://doi.org/10.3390/nitrogen2020016

[12] Aizawa T., Rsadi I., Yunata E. E., High density RF-DC plasma nitriding under optimized conditions by plasma diagnosis. Appl. Sci. 12, 3706 (2022) pp. 1-12. https://doi.org/10.3390/app12083706

[13] He K., Chen N., Wang C., Wei L., Chen J., Method for determining crystal grain size by X-ray diffraction. Crystal Res. Technol. 53 (1) (2018) 157. https://doi.org/10.1002/crat.201700157

[14] Frueh P., Heine A., Weber K. E., Wickert M., Effective depth-of-penetration range due to hardness variation for different lots of nominally identical target material. Defence Technol. 12 (2) (2016) pp. 171-176. https://doi.org/10.1016/j.dt.2015.10.002

[15] Fu J., Lyu D., Zhao J., Tribological characteristics of hard-to-hard matching materials of cylinder block/valve plate interface in electro-hydrostatic actuator pumps. J. Mech. Eng. Sci. 27 (2023) 61-68.

[16] Aizawa T., Shiratori T., Komatsu T., Integrated manufacturing of fine-grained stainless steels for industries and medicals. Chapter 1 in Engineering Steels and High Entropy-Alloys. IntechOpen, London, UK (2020) pp. 3-26. https://doi.org/10.5772/intechopen.89754

[17] Aizawa T., Micro-/meso-structure control of multi-hostmetal alloys by massive nitrogen supersaturation. J. Materials (2024) (in press). https://doi.org/10.3390/ma17061294

[18] Funazuka T., Horiuchi S., Dohda K., Shiratori T., Effect of CoCrMo die with nanotexture applied on micro-extrudability of micro backward extrusion of AA6063. Proc. WCMNM2023 (19th September, 2023; Evanston, Chicago, USA) 2023; 1-4.

[19] Silicolloy, https://www.silicolloy.co.jp/tribology/friction_wear_ballon-suj2/. (Retrieved at 2023/12/15).